The Meteoritical Society

Meteoritics & Planetary Science 55, Nr 5, 1057–1072 (2020)
doi: 10.1111/maps.13488

Convective activity in a Martian magma chamber recorded by P-zoning in Tissint olivine

N. MARI*, L. J. HALLIS, L. DALY, and M. R. LEE

School of Geographical and Earth Sciences, University of Glasgow, Glasgow G12 8QQ, UK
*Corresponding author. E-mail: n.mari.1@research.gla.ac.uk

(Received 17 August 2018; revision accepted 07 April 2020)

Abstract–The Tissint Martian meteorite is an unusual depleted olivine-phyric shergottite, reportedly sourced from a mantle-derived melt within a deep magma chamber. Here, we report major and trace element data for Tissint olivine and pyroxene, and use these data to provide new insights into the dynamics of the Tissint magma chamber. The presence of irregularly spaced oscillatory phosphorous (P)-rich bands in olivine, along with geochemical evidence indicative of a closed magmatic system, implies that the olivine grains were subject to solute trapping caused by vigorous crystal convection within the Tissint magma chamber. Calculated equilibration temperatures for the earliest crystallizing (antecrystic) olivine cores suggest a Tissint magma source temperature of 1680 °C, and a local Martian mantle temperature of 1560 °C during the late Amazonian—the latter being consistent with the ambient mantle temperature of Archean Earth.

INTRODUCTION

The Tissint Martian Meteorite

Tissint is one of the least terrestrially weathered Martian meteorites, having been seen to fall in Morocco in 2011 (Irving et al. 2012), and collected shortly after ~4 months (Chennaoui Aoudjehane et al. 2012). Tissint's crystallization age is 574 ± 20 Ma, based on Rb–Sr and Sm–Nd isotopic systematics (Brennecka et al. 2014), making it one of the oldest known shergottites. However, its cosmic ray exposure is in line with some other shergottite meteorites, at 1.05 Ma (Brennecka et al. 2014).

Tissint is an olivine-phyric shergottite, which exhibits large olivine crystals (up to 2 mm diameter), commonly containing melt inclusions (Balta et al. 2015). Plagioclase is completely converted to maskelynite, and shock produced melt glass is observed within Tissint, consistent with a peak shock pressure ⩾29–30 GPa (Walton et al. 2014), suggesting post-shock temperatures of ~200 °C for the whole rock (Stöffler et al. 1991). Low-Ca clinopyroxene (pigeonite) phenocrysts evolve to augite toward the rims, and subsequently to a high-Fe composition at the very end of crystallization (Balta et al. 2015). Oxides include ilmenite, ulvospinel, magnetite, and chromite, and rare pyrrhotite is also present. Phosphate is present in the form of merrillite only—no apatite has been reported (Balta et al. 2015). A fine-grained (<0.25 mm size) olivine- and clinopyroxene-rich mesostasis is observed (Balta et al. 2015; Liu et al. 2016).

Tissint is an unusual depleted olivine-phyric shergottite, characterized by a whole rock that is depleted in LREE and has a flat HREE pattern indicative of a mantle-derived melt (Balta et al. 2015). Petrogenetic calculations have located the depth of the Tissint magma chamber at ~40 to 80 km, corresponding to a pressure of ~4 kbar within the Martian upper mantle (Basu Sarbadhikari et al. 2016).

Mineral Chemistry as a Probe for Martian Magma Dynamics

Paleo-heat flows deduced from lithospheric strength suggest that the "stagnant-lid" tectonic regime of Mars has enabled mantle heat retention for the majority of the planet's history (Hauck and Phillips 2002; Breuer and Spohn 2006; Fraeman and Korenaga 2010; Grott and Breuer 2010; Ruiz et al. 2011). Mars' present-day

partially fluid core (e.g., Yoder et al. 2003) is further evidence for inefficient cooling of the Martian interior. Ages for the Martian surface derived from crater counting (Berman and Hartmann 2002), as well as the crystallization ages of shergottites as young as 175 Ma (Nyquist et al. 2001; McSween 2002), suggest that Mars could still be an episodically volcanically active planet (Carr and Head 2010).

Observations of chemical–physical variations in minerals within the shergottite group of Martian meteorites can be used to reveal the temperature and, by inference, the degree of convective activity of their respective magma chambers. Mg-Fe zoning of pyroxene has also been widely used to infer evolution of magmas after partial melting or metamorphism on asteroids (e.g., Hollister and Hargraves 1970; Duncan and Preston 1980; Scott 1980; Barton et al. 1982; Miyamoto et al. 1985; Spear and Markussen 1997; Mikouchi et al. 1999; Meado et al. 2017).

In addition, zoning of phosphorus in olivine is an effective tool to explore variations in crystal growth rate in magmatic systems (e.g., Milman-Barris et al. 2008; Shearer et al. 2013). Phosphorus behaves as an incompatible element (Toplis et al. 1994). However, during rapid growth, olivine can incorporate high concentrations of phosphorus (up to 0.48 wt% P_2O_5 in experimental products [Milman-Barris et al. 2008]) in its crystal structure via solute trapping (Aziz 1982; Reitano et al. 1994; Milman-Barris et al. 2008; Shearer et al. 2013; Bouvet de Maisonneuve et al. 2016; McCanta et al. 2016). The maximum P_2O_5 content recorded for terrestrial olivine is 0.2 wt%, whereas the maximum P_2O_5 content observed in Martian meteorite olivine is 0.4 wt% (Milman-Barris et al. 2008).

Here, we report major and trace element data for Tissint olivine and pyroxene. We focus on the core to rim compositional evolution of pyroxene and olivine in order to provide new insights into the dynamics of Tissint's parental magma chamber. Based on these results, equilibration temperature calculations in olivine are used to estimate the thermal state of the Martian mantle at the time of Tissint's formation.

ANALYTICAL METHODS

A total of four Tissint epoxy-mounted polished thick slices were investigated during this study (P18492, P18494, P18495, and P18497), on loan from the Natural History Museum of London, and cut from Tissint sample BM2012,M3.

Modal mineralogy was calculated by using the Aztec software on backscattered electron images. Major element mineral chemical data and X-ray elemental images were collected at the Imaging Spectroscopy and Analysis Centre of the University of Glasgow, using a Zeiss-Sigma variable pressure field emission gun scanning electron microscope (VP-FEG-SEM). Energy dispersive X-ray spectroscopy (EDS) data were collected using Oxford Instruments X-Max 80 mm^2 Silicon Drift Detector. These data were processed using Oxford Instruments Aztec 3.3 and INCA software. EDS and SEM data were acquired using a working distance of 8.5 mm, a beam current of 2.15 nA, and an accelerating voltage of 20 kV. EDS X-ray spectra were calibrated using reference materials of wollastonite (Si, Ca), jadeite (Na, Al), periclase (Mg), orthoclase (K), rutile (Ti), chromite (Cr), rhodonite (Mn), hematite (Fe), apatite (P), tugtupite (Cl), and pyrite (S), following the procedures outlined in Hallis et al. (2017). Major elements for olivine and pyroxene, collected via SEM-EDS, were used as input for equilibration temperature calculations following the method described in Putirka (2008).

Electron microprobe analyses (EMPA) of olivine were made on the JEOL 8530F field emission gun electron microprobe equipped with five tuneable wavelength dispersive (WD) spectrometers at the Centre for Microscopy, Characterisation and Analysis at the University of Western Australia. P-chemical profiles (elemental P) were collected across two olivine megacrysts (~2 to 2.5 mm) and two other, much smaller, olivine phenocrysts (~300 μm) in Tissint. WD data were collected using a fully focussed beam with a takeoff angle of 40°, 15 keV accelerating voltage, and a 50 nA beam current. The beam current was measured with a Faraday cup. The Kα peaks for elements Na, Si, Al, Mg, Cr, Mn, Fe, K, Ca, Ti, Ni, and P were measured using analyzing crystals LiF (Cr, Ti), PETJ (K, Ca, P), and TAP (Na, Si, Al, Mg) and quantified using reference materials of Durango apatite (P and Ca), Ni-olivine (Ni), rutile (Ti), orthoclase (Si and K), magnetite (Fe), Cr_2O_3 (Cr), periclase (Mg), spessartine (Mn), corundum (Al), and jadeite (Na). Beam-sensitive elements, such as Na, were measured first to minimize element loss. For all elements for both standards and unknowns, peaks were counted for 20 s. Intensity data were corrected for time-dependent intensity loss (or gain) using a self-calibrated correction for Na, Si, Cr, Mn, and K. The mean atomic number background correction was used throughout (Donovan and Tingle 1996; Donovan et al. 2016). Oxygen was calculated by cation stoichiometry and included in the matrix correction. The matrix correction method was Phi-Rho-Z (Armstrong 1988). Unknown and standard intensities were corrected for dead time. Interference corrections were applied to Mg for interference by Ca, to Mn for interference by Cr, and to Fe for interference by Mn (Donovan et al. 1993). Detection limits, based on 3σ,

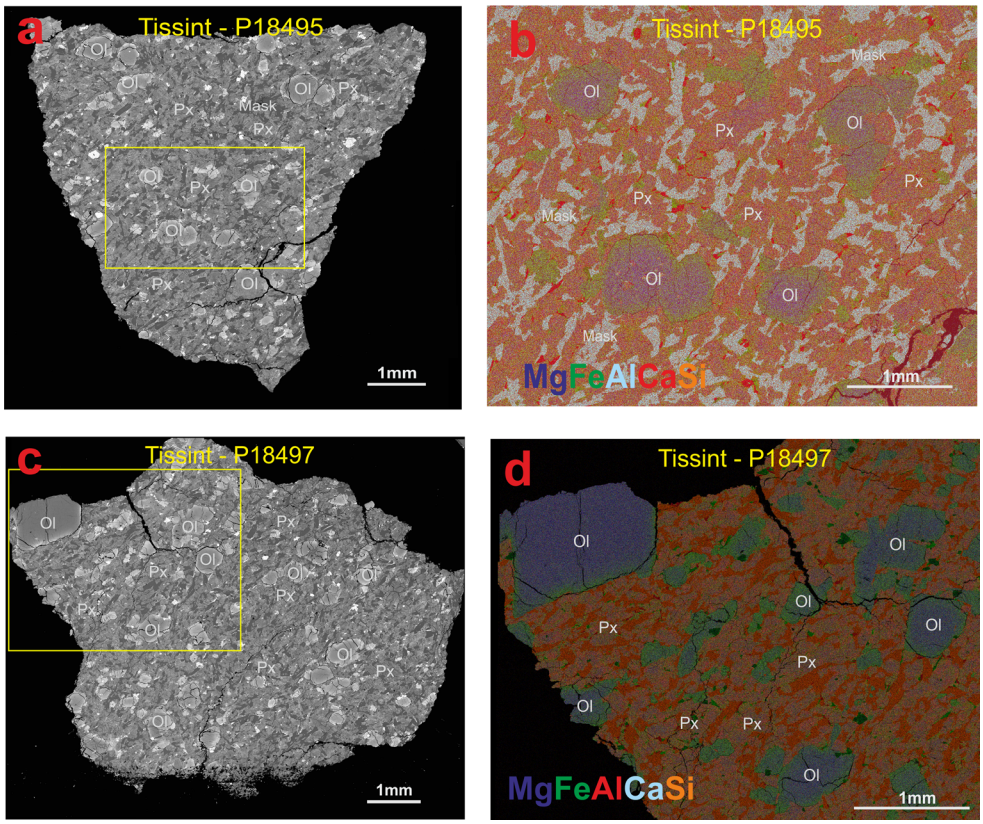

Fig. 1. BSE images (a, c) and false-colored X-ray images (b, d) of two Tissint thin sections (P18495 and P18497) analyzed during this study. a) BSE image of Tissint (P18495). The yellow box corresponds to the area shown in (b). b) False-colored EDS map of Tissint, Mg (blue), Fe (green), Al (aqua), Ca (red), and Si (orange), highlighting olivine (Ol) phenocrysts within intergrown pyroxene (Px) and maskelynite (Mask). c) BSE image of Tissint (P18497) with fusion crust visible at the bottom of the section. The yellow box corresponds to the area shown in (d). d) False-colored EDS map of Tissint, Mg (blue), Fe (green), Al (red), Ca (aqua), and Si (orange), highlighting a large olivine megacryst at the top left corner of the sample. (Color figure can be viewed at wileyonlinelibrary.com.)

were 0.004 wt% for Al, 0.005 wt% for Mg, 0.008 wt% for Na, 0.010 wt% for Fe, 0.028 wt% for Ti, and 0.009 wt% for P. Analytical uncertainties for each measurement were variable but are generally better than 0.3% for major elements (>1 wt%) and better than 20% for trace elements (<0.1 wt%).

Abundances of Ni and Co were measured using an iCAP-RQ inductively coupled plasma-mass spectrometer (ICP-MS), equipped with a RESOlution 193 nm Excimer laser, at the University of Glasgow. Data were collected from two olivine megacrysts and several phenocrysts (divided into Mg-rich, Mg-poor, and intermediate), pyroxene (both pigeonite and augite), and low-Ti chromite. We analyzed a NIST 612 glass standard throughout each analytical session (at the session beginning, end, and after every third analysis). An Ar gas carrier was utilized, and the dwell time for each laser analysis was 0.35 s. In order to avoid low signal, we chose a different laser spot size for the different minerals analyzed: 10 μm for Ni and Co in olivine and 20 μm for pyroxene and chromite. NIST standards were always analyzed with the same laser spot size as the analyses. Uncertainties are calculated based on the standard deviation of NIST analyses, and are reported in the supporting information. Elemental abundances were calculated using the GeoStar software, while data processing was performed using Iolite data reduction analytical software, by quantifying the trace element abundances in the flat regions of the time-lapse plots. The detection limit for Ni is 0.025 ppm, while that for Co is 0.037 ppm.

RESULTS

Petrography

Tissint has a porphyritic texture (Fig. 1), olivine megacrysts (up to 2.5 mm), and smaller phenocrysts (up to 0.8 mm; Fig. 2). The average modal mineralogy of all four samples is 55 vol% pyroxene, 25 vol% olivine,

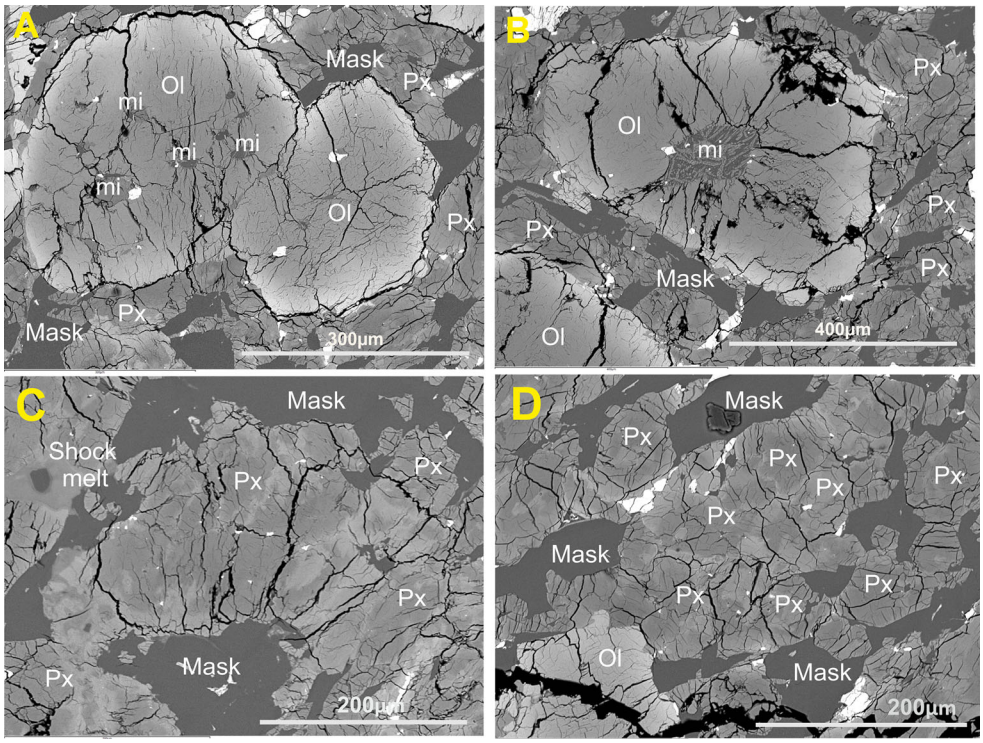

Fig. 2. BSE images of olivine (Ol) and pyroxene (Px) phenocrysts in Tissint. All grains are heavily fractured. A) A cluster of two euhedral olivine phenocrysts, the upper left of which contains numerous melt inclusions (mi). B) A euhedral olivine phenocryst with large melt inclusion. C) A large area of pyroxene, where Fe-rich pyroxene appears to penetrate through areas of augitic composition. An area of shock-melted pyroxene is highlighted in the top left of the image. D) Clusters of augite grains surrounded by Fe-rich pyroxene, and penetrated by a high density of fractures. Maskelynite (Mask) is present within the gaps between pyroxene clusters. White grains are oxides. (Color figure can be viewed at wileyonlinelibrary.com.)

and 15 vol% maskelynite. The remaining 5 vol% includes chromite, merrillite, ilmenite, pyrrhotite, and mesostasis. These observations are in agreement with previously published data (Balta et al. 2015; Liu et al. 2016).

Olivine in Tissint includes megacrysts (~2 mm diameter) and phenocrysts (~200 μm diameter; Figs. 1 and 2). The textures of olivine phenocrysts are variable: many are fractured, and contain a high abundance of melt inclusions and oxides (mostly spinel). The olivine grains are often observed in clusters of two or three (Fig. 2a), in agreement with previous observations of olivine clustering in Tissint (e.g., Liu et al. 2016; Fig. 2). Conversely, olivine megacrysts, the largest of which is >2.5 mm diameter (cutoff at the sample edge), are not clustered, although this may be due to sampling bias as only two megacrysts are present within the four samples studied. The olivine megacrysts reported in this work are among the largest detected in Tissint.

The earliest crystallizing pyroxene (cores of the largest grains) is pigeonite, which becomes augite toward the rims. Smaller phenocrysts are entirely made up of augite (see Fig. 6). Fe-rich pyroxene (augitic) rims surround each pyroxene phenocryst. Plagioclase has all been converted to maskelynite, which is intergrown with pyroxene. Olivine and pyroxene are heavily shock fractured, and shock melting is evident in some regions (Fig. 2c).

Mineral Chemistry

Olivine Major and Minor Elements

Both megacrysts (n = 2) and phenocrysts (n = 26) of olivine exhibit normal zoning, from Mg-rich cores to Fe-rich rims. The abundance of MgO in olivine is variable (37–29 wt%) and correlates with the crystal size—the cores of the larger olivine megacrysts are more Mg-rich than the olivine phenocrysts. Olivine megacryst composition ranges from Fo_{73} in the cores to Fo_{40} in the rims, while the olivine phenocrysts range from Fo_{66} in the cores to Fo_{22} in the rims (Figs. 2 and 6).

Olivine megacrysts have low P_2O_5 abundances (~0.02 to 0.03 wt%) in their cores and rims, with P_2O_5 concentration increasing toward the very outer rims (~0.5 wt%). The olivine phenocrysts have higher

Table 1. SEM-EDS major elements and LA-ICP-MS trace elements composition of representative Tissint minerals and phases.

	Olivine megacryst		Olivine phenocryst		Pigeonite			
wt%	Core	Rim	Core	Rim	Core	Rim	Maskelynite	Chromite
SiO_2	39.34	36.37	35.82	34.27	53.37	50.49	51.82	0.35
TiO_2	–	–	0.05	–	0.16	0.71	0.11	0.72
Al_2O_3	0.21	0.23	0.26	0.16	0.90	1.06	29.37	7.65
Cr_2O_3	0.24	0.52	0.16	0.04	0.51	0.34	0.04	58.35
MgO	42.62	33.44	32.71	24.00	22.57	14.51	0.17	7.29
CaO	0.22	0.24	0.25	0.37	4.34	8.79	12.98	0.04
MnO	0.34	0.53	0.53	0.74	0.56	0.74	0.03	0.67
FeO	17.84	26.99	28.09	39.64	15.78	23.28	0.78	24.88
NiO	–	–	–	–	0.03	–	0.12	–
Na_2O	0.13	0.10	0.16	0.07	0.17	0.11	3.54	0.10
K_2O	–	–	–	–	0.05	0.00	0.00	0.01
P_2O_5	0.01	0.07	0.08	0.03	0.04	0.05	–	0.04
S_2	–	–	–	–	0.03	0.10	–	–
Total	100.95	98.5	98.25	99.32	98.52	100.18	98.96	100.08
Mg#	70.49	55.33	53.79	37.71	58.85	38.39	–	–
En	–	–	–	–	52.86	31.15	–	–
Wo	–	–	–	–	10.16	18.87	–	–
ppm	Core	Rim	Mg-rich	Fe-rich	Mg-rich	Ca-rich		
Ni	13.7	13.2	9.9	1.78	1.94	1.63	–	1.81
Co	1.51	1.47	1.27	0.73	0.62	0.52	–	1.42

Wo = 100 × Ca/(Ca + Mg+Fe^{2+}); En = 100 × Mg/(Ca + Mg + Fe^{2+}); Mg# = 100 × Mg/(Fe + Mg).

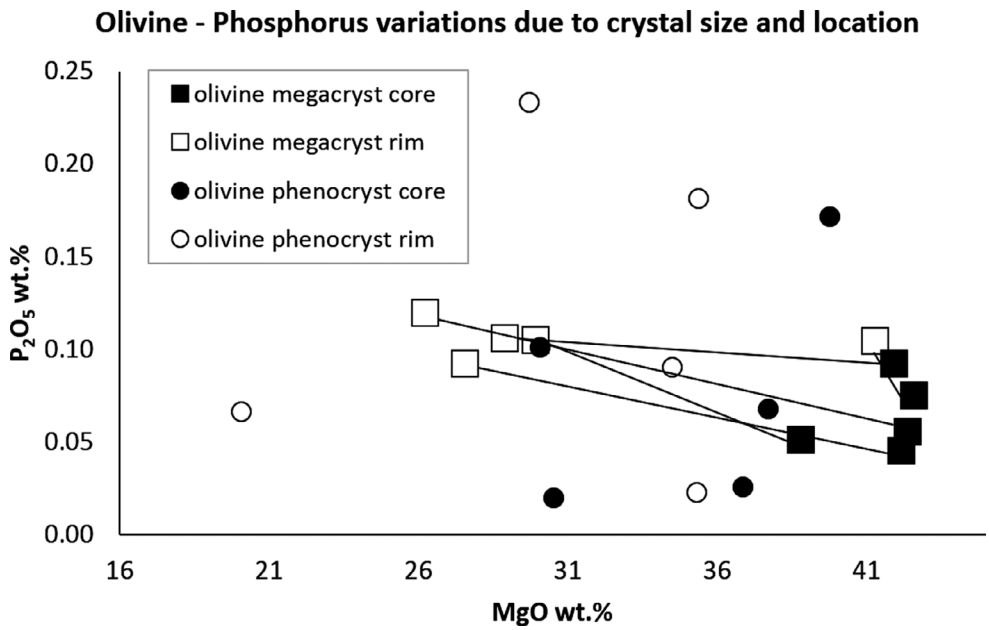

Fig. 3. A plot showing P_2O_5 versus MgO (both in wt %) collected via SEM-EDS, depicting the chemical variations between the rim and core of both olivine phenocrysts (n = 5) and megacrysts (n = 5) in Tissint. The olivine megacrysts have a slight rimward enrichment in P_2O_5 and depletion in MgO. Conversely, the olivine phenocrysts exhibit no trend in the concentration of P_2O_5 with proximity to the core or rim, and exhibit a larger variability in P_2O_5. Lines link cores and rims of individual olivine megacrysts.

concentrations of P_2O_5 independently of their cores and rims (ranging from ~0.02 to 0.23 wt%, without any variations from core to rim; Table 1, Fig. 3). The high concentration of P_2O_5 in the outer olivine rims is likely related to cooling during lava flow emplacement (Basu Sarbadhikari et al. 2017).

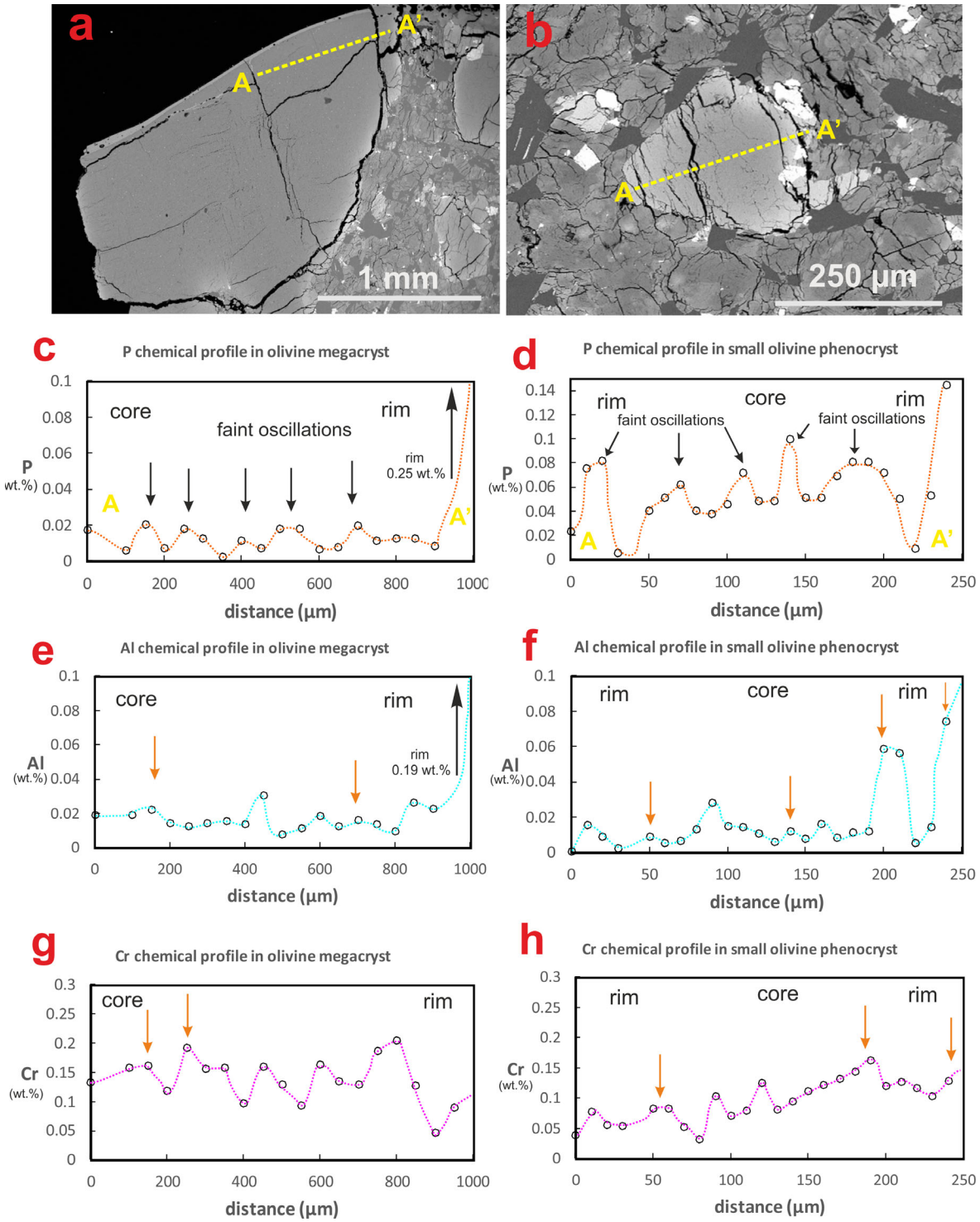

Fig. 4. BSE images (a, b) along with P (c, d), Al (e, f), and Cr (g, h) chemical profiles for an olivine megacryst and a small olivine phenocryst in Tissint. The yellow dashed lines between A and A′ represent the analytical transects. Axis value is different for some figures in order to enhance oscillations visualization. Direct correlations of Al and Cr with P are highlighted by orange arrows. The megacryst transect (a) shows oscillations in P content (black arrows), with spacings of ~200 µm and band widths of ~40 to 50 µm (c). A great increase in P up to 0.25 wt% is detected at the rim (not shown here). The olivine phenocryst (b) shows stronger P oscillations (d), with a generally higher P content. Oscillations are visible in Al (e, f) and Cr (g, h), and direct correlation of Al and Cr with P is shown (orange arrows). Data obtained using EMPA. (Color figure can be viewed at wile yonlinelibrary.com.)

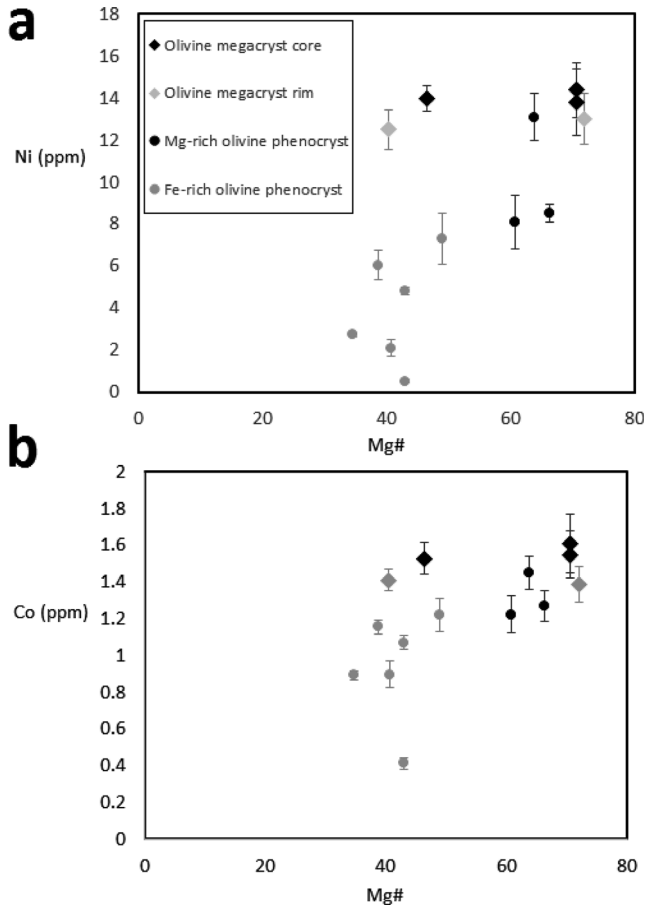

Fig. 5. Mg# versus Ni (a) and Co (b) ppm of olivine megacrysts (cores and rims), alongside Mg-rich and Fe-rich olivine phenocrysts. Elevated Ni and Co abundances within the megacryst cores in particular indicate they represent an earlier crystallizing population to the olivine phenocrysts, as both Ni and Co are compatible in olivine. Error bars represent the 2σ errors of LA-ICP-MS analyses for Ni and Co.

EMPA data were collected along a transect through one olivine megacryst and across one phenocryst. Within both the megacryst and the phenocryst P is distributed in bands with an oscillatory abundance—as also observed by Balta et al. (2015) and Liu et al. (2016). The olivine megacryst has P-rich bands 40–50 μm wide and ~200 μm apart, with increasing P enrichment at the very rim of the grain (Fig. 4c). The olivine phenocryst has P-rich bands of a similar width (20–50 μm wide), but much closer together at ~25 μm apart—it also has a P enrichment at the very rim of the grain (Fig. 4d).

In addition to P, chemical profiles were collected for Al and Cr (Fig. 4), because all three elements have similar diffusion coefficients (e.g., Watson et al. 2015). In terrestrial olivines Cr and Al, oscillatory zoning is generally weak or absent, but a previous study reported a positive correlation between Al-, Cr-, and P-rich bands within synthetic and extraterrestrial olivine (Milman-Barris et al. 2008), although these oscillations are noted to never correlate to Fe-Mg major element zoning. Tissint olivine shows a slight correlation of P-rich bands with Al-rich bands, but little correlation with Cr-rich bands, although the olivine megacryst does show definite oscillations in Cr content (Fig. 4g).

In the olivine megacrysts and phenocrysts, abundances of P, Al, and Cr vary significantly, but the variations are only partially correlated. The olivine megacryst profile runs from core to rim, a distance of 1000 μm. A direct correlation between P and Al is detected at 180, 700, and 1000 μm (Fig. 4), with the rims having the highest abundance of P (0.25 wt%) and Al (0.19 wt%). A direct correlation between P and Cr is only located at 180 and 250 μm, with no large enrichment in Cr at the rim. The same degree of correlation within P- and Al-rich bands is observable for the chemical profile of the olivine phenocryst. Here, the profile goes from rim to rim, with a total distance of 250 μm. Al-rich bands are directly correlated with P-rich bands at 50, 140, 200, and 240 μm distance, with an enrichment on both rims (up to 0.14 wt% P and 0.08 wt% Al). Correlations between Cr-rich bands and P-rich bands are shown at 60, 180, and 240 μm in the phenocryst. However, anticorrelations are also present in both grains, with the olivine megacryst being enriched in P but depleted in Al at 300, 500, and 900 μm, and the phenocryst showing the same trend at 110 μm. A decrease in P is associated with increasing in Al and Cr at 90, 160 μm within the phenocryst.

Olivine Trace Elements

Ni and Co are more abundant in olivine megacrysts than olivine phenocrysts (Fig. 5). Only the most Mg-rich phenocrysts approach the Ni and Co abundances of the megacrysts. Ni and Co contents in olivine megacrysts are constants from core to rims (Ni 14.4–12.5 ppm and Co 1.6–1.4 ppm for both). In contrast, Ni is more abundant in Mg-rich phenocrysts (13.1–8.52 ppm) than in Fe-rich phenocrysts (2.74–0.52 ppm), as is Co (1.45–1.23 ppm in Mg-rich versus 0.9–0.4 ppm in Fe-rich olivine; Table 1, Fig. 5).

Chromite Inclusions in Olivine

Chromite occurs as inclusions only in the olivine phenocrysts (both in cores and rims) and not in the olivine megacrysts. Analyses of these chromite grains show an increase in TiO_2 (0.68–1.16 wt%) and a

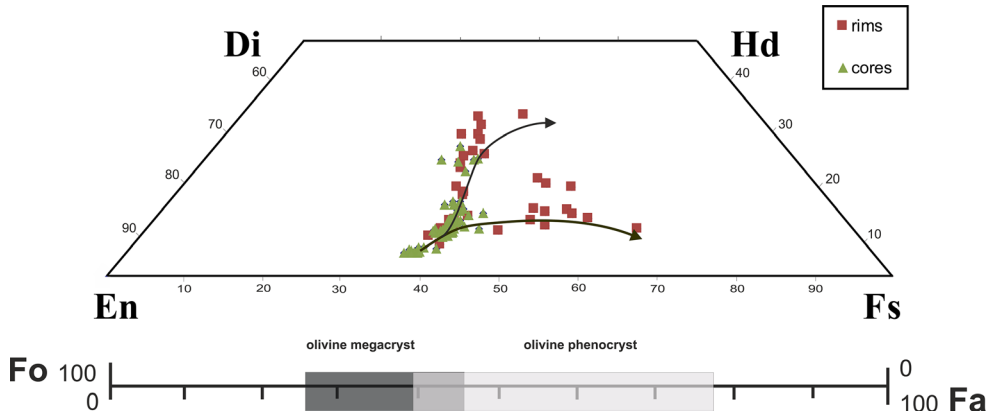

Fig. 6. Core to rim compositional variation for pyroxene and olivine composition in Tissint. Chemical data were collected via SEM-EDS. Two zoning patterns are present in pyroxene: from Mg-rich cores to Fe-rich rims, and from Mg-rich cores toward Fe-Ca-rich rims. Olivine megacrysts (black box) and phenocrysts (gray box) are displayed in terms of percentage of Fo versus Fa. Abbreviations: Di, diopside; Hd, hedenbergite; En, enstatite; Fs, ferrosilite; Fo, forsterite; Fa, fayalite. (Color figure can be viewed at wileyonlinelibrary.com.)

decrease in Cr_2O_3 (59–55 wt%) toward the rim of each grain. Na and Fe also increase toward the grain rims, to a maximum of ~0.23 wt% Na_2O and ~30.8 wt% FeO. Trace element data indicate that Ni is slightly more abundant than Co (1.81 and 1.42 ppm, respectively).

Pyroxene Major and Minor Elements

The morphology of the majority of Tissint pyroxene phenocrysts is subhedral, with rare euhedral exceptions (Fig. 2). Pyroxene phenocryst grain size varies from 80 to 200 μm along the short axis and from 0.1 to 0.8 mm along the long axis ($n = 20$). Compositional variation from Mg-rich to Fe-rich pyroxene exists in both pigeonite ($En_{51}Wo_{10}$) and augite ($En_{44}Wo_{16}$) grains (Table 1, Fig. 6). Mg-rich pigeonite has slightly elevated Co and Ni (0.43–0.82 ppm and 0.98–2.9 ppm, respectively) compared to Ca-rich pigeonite (0.49–0.56 ppm, and 0.95–2.32 ppm, respectively; Table 1).

DISCUSSION

Origin of P-Zoning in Olivine

P-zoning in Tissint olivine is comparable to previously reported P-oscillatory zoning in olivine grains in other olivine-phyric shergottites (Shearer et al. 2013; Ennis and McSween 2014; Jean et al. 2017). Previously reported P_2O_5 abundances for Tissint olivine phenocrysts range from below EMPA detection limits in the cores (<0.02 wt%) to 0.2 wt% in the rims (Balta et al. 2015; Liu et al. 2016).

Oscillatory zoning in phosphorus content in olivine and pyroxene is rare on Earth (Thompson 1972; Downes 1974; Eriksson 1985; Clark et al. 1986; Pearcea and Kolisnik 1990; Simonetti et al. 1996; Cioni et al. 1998; Milman-Barris et al. 2008; Shearer et al. 2013) and is thought to be inconsistent with compositional changes due to open-system processes in magma chambers (Clark et al. 1986). In addition to Tissint, phosphorus zoning in Martian olivine is reported in Yamato 980459, Northwest Africa (NWA) 1183, Allan Hills (ALHA) 77005, Elephant Moraine (EETA) 79001, Dar al Gani (DaG) 476, and Dhofar 019 (Milman-Barris et al. 2008; Shearer et al. 2013; Ennis and McSween 2014). These Martian meteorites have varying degrees of depletion (in light rare earth elements and other highly incompatible elements), suggesting that P-oscillatory zoning is not linked to the degree of melt depletion. Milman-Barris et al. (2008) reproduced olivine P-oscillatory zoning in experimental products, but the olivine produced experimentally contained regularly spaced fine bands, unlike the irregularly spaced wide bands in Tissint and other natural samples (e.g., Balta et al. 2015; Elardo and Shearer 2014).

Phosphorus oscillatory zoning can be interpreted as the product of intrinsic or extrinsic phenomena in the magmatic system (Pearce 1994; Shore and Fowler 1996). Intrinsic processes would include crystallization kinetics and can occur without change in the P content of the magma. For example, if the crystal growth rate exceeds the diffusion of P in the melt (a chemical process known as solute trapping; Aziz 1982), oscillatory zoning would form due to incorporation of P in the crystals, probably in relation to undercooling in the magma chamber (Aziz 1982; Pearce 1994; Reitano et al. 1994; Lofgren et al. 2006; Milman-Barris et al. 2008). Oscillatory zoning can be caused by changes in melt

chemical composition induced by external processes, such as magma mixing and magmatic replenishment events (Pearce 1994; Shore and Fowler 1996; Cioni et al. 1998; Reubi et al. 2003; Milman-Barris et al. 2008). These extrinsic processes would also typically generate characteristic resorption bands, reflecting the injection of more primitive magma into the magma chamber (Pearce 1994; Ginibre et al. 2002). Intrinsic solute trapping commonly produces finely banded (~10 to 20 μm) regular or irregular P-oscillatory zoning (Milman-Barris et al. 2008), while extrinsic magma mixing or replenishment produces coarse and mostly irregular banding (Pearce 1994). Oscillations in abundances of P are apparent throughout the Tissint megacryst and phenocryst olivine grains, from core to rim. In contrast, P-zoning of terrestrial olivine normally appears as a P-rich core surrounded by a P-poor rim or mantle (Milman-Barris et al. 2008). Olivine megacryst cores analyzed in Y-980459 are P-rich but with higher Mg#, V, and Ti relative to the Y-980459 olivine phenocrysts, implying a xenocrystic origin for the megacrysts; thus, P-oscillatory zoning was caused by magma mixing (Shearer et al. 2013). P-poor cores were reported in the enriched shergottite NWA 1183 olivine megacrysts, surrounded by phosphorus oscillatory bands in which P is correlated with Al (Shearer et al. 2013). NWA 1183 is reported to have crystallized in a closed system from a single melt (Shearer et al. 2013).

Milman-Barris et al. (2008) produced regularly spaced P-zoning in olivine during constant cooling rate experiments. However, they also report that in natural samples, oscillatory P-zoning is irregularly spaced, as a consequence of irregular variations in temperature and cooling rates. Milman-Barris et al. (2008) thus argued that irregularly spaced P zoning in natural olivine may be related to solute trapping during cooling events, probably due to convection in a magmatic system.

Evidence of Equilibrium Crystallization in a Closed System

As well as the size disparity between the megacrysts and phenocrysts, differences in Mg, Ni, and Co abundances indicate the presence of two distinct olivine populations (Fig. 5; Table 1). The cores of the megacrysts are richer in Mg, Ni, and Co, indicating early crystallization. The total separation of core versus rim in terms of megacryst MgO content, in contrast to the gradual evolution shown by the phenocrysts, suggests a gap in crystallization between the core and rim development. In addition, the presence of thin P-rich rims on the olivine megacryst studied via EMPA (Figs. 3 and 4) suggests a second, short, growth stage at the end of crystallization. Therefore, the olivine megacrysts appear to have evolved as antecrysts—defined as phenocrysts that crystallize from a magma chemically similar to the sample groundmass, which subsequently spend time in a cumulate pile environment prior to entering the magma chamber system (Davidson et al. 2007; Jerram and Martin 2008). This conclusion is in agreement with Balta et al. (2015) and Liu et al. (2016). As suggested by Balta et al. (2015), the presence of olivine antecrysts combined with the relatively young age of Tissint could be an important constraint for a long-term active magmatic system on Mars during the last few hundred Ma.

The presence of chromite only in the olivine phenocrysts and not in the antecrysts supports the presence of two separate olivine populations. In fact, it is unlikely that the antecrysts could have reached the liquidus before chromite. Previous authors used the olivine-pyroxene-chromite assemblage to calculate a subliquidus temperature close to 1200°C and a fO_2 close to QFM-4 for Tissint (Balta et al. 2015). These data were used to determine a crystallization sequence that included chromite crystallization prior to olivine in contrast to other olivine-phyric shergottites (Balta et al. 2015). The absence of chromite in Tissint olivine antecrysts can thus only be explained by an antecrystic origin—that is, crystallization in a previous melt of the same active magmatic system and then accumulation and entrainment in the final host magma (Balta et al. 2013).

Changes in fO_2 may have impacted the final trace element zoning of the olivine. Experimental studies under known cooling rates evidenced a noticeable increase in oxygen fugacity in the Tissint magma, from ~3.5 log units below the quartz–fayalite–magnetite (QFM) buffer to QFM-1.4 (Castle and Herd 2017). These significant changes in fO^2 may have overprinted some of the original magmatic zoning of Cr and P in the Tissint olivine (Castle and Herd 2017, 2018), possibly explaining the missing correlation between Cr and P in some of the areas of the EMPA transects displayed in Fig. 4.

The two trends of pyroxene crystallization as represented in Fig. 6 reflect a normal condition of magmatic evolution in a magma chamber, with high-Ca augites as the product of later crystallization in the same magma (e.g., Poldervaart and Hess 1951). The elevated Co and Ni in Mg-rich pyroxene in respect to Ca-rich pyroxene (Table 1) reflects the onset of pigeonite crystallization prior to that of augite, as both Co and Ni are compatible in pyroxene. These observations imply an absence of dominant open-system processes that would influence pyroxene chemistry from core to rim.

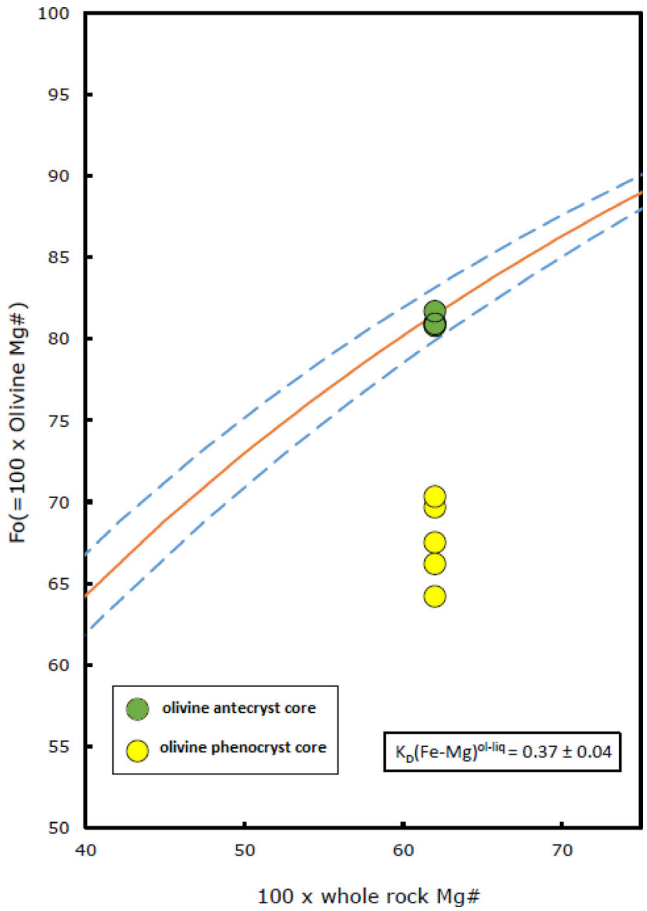

Fig. 7. Rhodes diagrams used to test for equilibrium for Tissint olivine antecryst cores and olivine phenocryst cores (Rhodes et al. 1979). Values in the continuous curves represent the experimentally deduced K_D(Fe-Mg) for olivine-liquid for Mars (Putirka 2016; equation 10a) while the dashed curves represent the error intervals of these values, as reported in captions for each diagram. Data are plotted from values reported in Table 2. Olivine antecryst cores are inside the equilibrium range; olivine phenocryst cores are displaced from this range. (Color figure can be viewed at wileyonlinelibrary.com.)

CONSTRAINT ON MARTIAN MANTLE CONVECTION AND TEMPERATURE

Equilibration Temperatures

To test for mineral equilibrium and to see whether magma mixing processes may have affected the magmatic system of Tissint, olivine-melt equilibration temperature (T_{eq}) calculations were performed. Equilibration temperature calculations were also performed for the Tissint Ca-rich and Mg-rich pyroxene compositions (see supporting information).

The test described by Roeder and Emslie (1970) was used for this purpose. An Fe-Mg exchange coefficient (K_D) of 0.37 ± 0.04 for Martian olivine and pyroxene was calculated by Putirka (2016) after >100 experiments using Martian melt compositions. This exchange coefficient is independent of fO_2 and other compositional parameters. This value was used as the exchange coefficient for both olivine ($K_D[Fe\text{-}Mg]^{ol\text{-}liq}$) and pyroxene ($K_D[Fe\text{-}Mg]^{px\text{-}liq}$). A Rhodes Diagram was used (Fig. 7) to determine whether each mineral was in equilibrium, based on displacement from the experimentally determined Martian Fe-Mg exchange coefficient curves (Rhodes et al. 1979). The Tissint basaltic glass data of Chennaoui Aoudjehane et al. (2012) were taken to represent the parental melt, while the cores of olivine and pyroxene were used as input for the mineral compositions. Calculated temperatures show an olivine T_{eq} range of 1641–1541 °C for a $K_D(Fe\text{-}Mg)^{ol\text{-}liq}$ of ~0.58, and a pyroxene T_{eq} range of 1562–1125 °C for a $K_D(Fe\text{-}Mg)^{px\text{-}liq}$ of ~0.32 (Table 2). Olivine antecryst cores were found to be in equilibrium with the melt based on these calculations (Fig. 7), while cores of olivine phenocrysts and pyroxene show slight disequilibrium with the melt (see supporting information), indicating that initial crystallization of these minerals occurred in different chemical conditions than the Tissint parental magma. This is commonly found also for pyroxene in terrestrial volcanic systems, where slight displacements from the experimentally derived curve are present without large disequilibrium between minerals and liquid (Putirka et al. 2007; Sheehan and Barclay 2016). Thus, here we use the core of the olivine antecrysts for mantle thermometrical calculations.

Vigorous Convection in the Tissint Magma Chamber

In the absence of open-system behavior for the Tissint magmatic system, an intrinsic process for the generation of olivine P-zoning in the Tissint magma chamber is required. The zoning of P in the smallest olivine and toward the rims of the largest grains is inferred to be a result of solute trapping, preserved by the slow diffusion rate of P in the melt in combination with a fast magma cooling rate. Solute trapping of P in the crystal structure occurs when the crystal growth rate exceeds the diffusion of P in the melt (Aziz 1982). Toplis et al. (1994) and Milman-Barris et al. (2008) inferred exactly this process to explain P zoning in laboratory-grown olivines. This process could be related to convection-induced differential cooling in the magma chamber (Martin et al. 1987). In order for oscillatory P-zoning to be present in olivines in terrestrial basalts, cooling rates of 15–30 °C h^{-1} are required in the magma chamber, as deduced from crystallization experiments (Milman-Barris et al. 2008). Magma

Table 2. Equilibration temperatures (T_{eq}) and Fe-Mg distribution coefficients (K_D) for selected Tissint olivine antecryst cores, olivine phenocryst cores, and Ca-rich and Mg-rich clinopyroxene. Elemental compositions of olivine and clinopyroxene were determined via SEM-EDS (expressed in wt%).

Phase	SiO_2	TiO_2	Al_2O_3	FeO	MnO	MgO	CaO	Na_2O	K_2O	Cr_2O_3	P_2O_5	T_{eq} (°C)[b]	K_D(Fe-Mg)$^{min\text{-}liq}$
Liquid[a] (Chennaoui Aoudjehane 2012)	44.86	0.56	4.09	21.84	0.51	19.99	6.03	0.63	0.04	0.81	0.46	–	–
Liquid (Herd et al. 2013)	47.20	0.67	5.20	21.60	0.56	16.00	7.00	0.77	–	–	0.51	–	–
Olivine antecryst	39.26	0.02	0.22	17.95	0.34	42.39	0.25	0.11	0.00	0.30	0.06	1541	0.388
Olivine antecryst	39.07	0.00	0.25	17.57	0.35	41.93	0.18	0.07	0.00	0.77	0.09	1541	0.384
Olivine antecryst	39.09	0.00	0.21	17.85	0.36	42.20	0.19	0.16	0.01	0.22	0.05	1541	0.387
Olivine antecryst	40.61	0.00	0.31	17.07	0.35	42.70	0.20	0.14	0.00	0.00	0.07	1542	0.366
Olivine antecryst	39.94	0.00	0.23	17.57	0.39	41.77	0.24	0.19	0.00	0.00	0.09	1545	0.385
Olivine phenocryst	35.82	0.05	0.26	28.09	0.53	32.71	0.25	0.16	0.00	0.16	0.08	1618	0.786
Olivine phenocryst	35.83	0.01	0.16	29.11	0.63	31.94	0.22	0.14	0.00	0.15	0.26	1628	0.834
Olivine phenocryst	35.81	0.00	0.29	26.33	0.45	33.90	0.28	0.15	0.00	0.21	0.23	1603	0.711
Olivine phenocryst	36.19	0.00	0.27	25.94	0.55	34.48	0.25	0.14	0.00	0.19	0.19	1600	0.689
Olivine phenocryst	35.19	0.01	0.20	30.48	0.61	30.64	0.31	0.14	0.00	0.08	0.01	1641	0.910
Ca-pyroxene	49.90	0.35	0.78	14.04	0.68	14.89	5.75	0.16	0.00	0.22	–	1125	0.272
Ca-pyroxene	52.94	0.20	1.39	14.16	0.53	18.46	12.36	0.15	0.00	0.84	–	1528	0.343
Ca-pyroxene	49.58	0.32	1.82	14.09	0.51	16.13	12.96	0.21	0.00	0.81	–	1551	0.346
Mg-pyroxene	52.54	0.12	0.87	17.08	0.53	22.58	3.72	0.14	0.00	0.50	–	1562	0.358
Mg-pyroxene	53.74	0.12	0.89	16.99	0.59	22.63	5.30	0.13	0.00	0.56	–	1382	0.322
Mg-pyroxene	51.64	0.22	1.00	16.66	0.62	20.85	6.05	0.11	0.00	0.69	–	1325	0.311

[a]Tissint melt composition is estimated based on the Tissint glass data of Chennaoui Aoudjehane et al. (2012), representing Tissint whole rock composition. T_{eq} and K_D(Fe-Mg) for olivine and pyroxene are calculated using the methods of Putirka et al. (2007) and Putirka (2008).

[b]The T_{eq} (°C) was calculated from Putirka et al. (2007; equation 4). This equation included element partition coefficients, pressure, water content, and other coefficients that were derived by nonlinear regression of experimental data (Beattie 1993; Putirka et al. 2007; Putirka 2008). For olivine T_{eq}, we used values of P(GPa) = 0.8 (Basu Sarbadhikari et al. 2016). For pyroxene T_{eq}, we used P(GPa) = 0.5 (Kinzler and Grove 1992).

chamber convection and changes in melt composition could have also contributed to oscillatory P-zoning in olivine, as these processes commonly result in oscillatory zoning in pyroxene (Elardo and Shearer 2014).

The process of solute trapping is evidenced also from the olivine chemical profiles. According to Grant and Kohn (2013), during normal elemental partitioning accompanying melt fractionation in olivine, P should show weak or not correlations with Al and Cr. Solute trapping is instead clearly evidenced when the P-rich bands are correlated to Al- and Cr-rich bands; we notice these correlations for part of the P-rich bands in the olivine megacryst and phenocryst in Fig. 4.

Considering all the above evidence, oscillatory P-zoning could have occurred due to transient fast cooling rates during vigorous convection. Following this logic, when olivine grains were in the cooler parts of the magma chamber (exterior walls and possibly upper region), they were likely affected by solute trapping, forming P-rich bands within the grains. When the same grains were removed via convection to hotter regions of the magma chamber (central or lower regions), solute trapping would cease and P-poor olivine bands would be produced (Fig. 8). In addition, Fe-rich pyroxene rims, even at boundaries with other pyroxene or olivine grains (Figs. 2d and 3), imply that the pyroxene grains did not settle or cluster until the very late stages of crystallization (e.g., Day et al. 2006).

Implications for the Thermal State of the Martian Mantle

Thermal evolution in a planetary body is likely controlled by, among other mechanisms, cooling induced by mantle convection and partial melting (Stevenson et al. 1983; Spohn 1991; Hauck and Phillips 2002; Fraeman and Korenaga 2010). Convection speeds in magma chambers of terrestrial volcanic systems have been estimated to range from ~ 0.5 mm s^{-1} for normal degrees of convection to ~ 0.3 m s^{-1} for vigorous convection (Moussallam et al. 2015; Carey et al. 2013). For comparison, the convection speed for the Earth's upper mantle is typically ~ 20 mm yr^{-1} (Liu et al. 2007; Takeuchi and Sugi 1971) with a complete convective cycle once every 50 Myr.

Below, we calculate the Tissint magma source temperature (Tp) using EDS chemical compositions

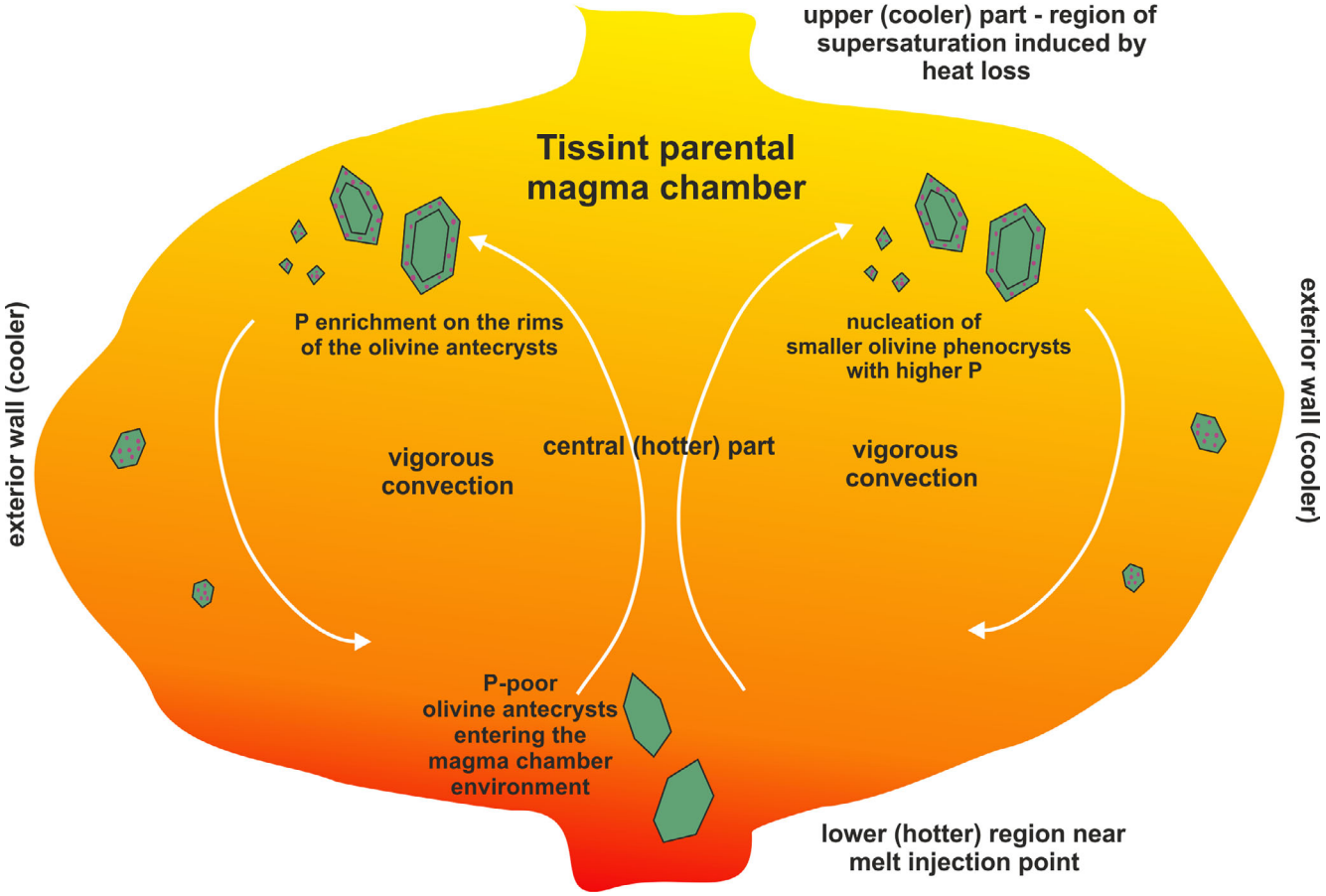

Fig. 8. Schematic representation of the convective activity present in the plume-fed Tissint parental magma chamber on Mars. Different thermal regions are defined: the lower region and central regions (hotter), the upper region (cooler, closer to the Martian crust), and the exterior walls (cooler). Cycling due to vigorous convection (here represented by the arrows) would bring olivine crystals (green) from hotter to cooler regions, and vice versa, causing P solute trapping (purple dots) while the olivine grains are cool, producing P-rich bands, which ceases when the olivine grains are in hotter regions of the magma chamber, producing P-poor bands. (Color figure can be viewed at wileyonlinelibrary.com.)

from Tissint olivine antecryst cores in equilibrium with the parental melt. The average equilibration temperature for olivine melt (Table 2) and an equilibration pressure of 8 kbar were consistent with the most accurate estimates of the depth of the Tissint magma chamber (~40 to 80 km; Basu Sarbadhikari et al. 2016). The following equation from Putirka (2008) was used for this purpose:

$$\text{Tissint magma } T\text{p} = T^{\text{ol-liq}}(^{\circ}\text{C}) + \left(\text{Melt fraction} \times \frac{\text{Heat of fusion } \left(\frac{\text{KJ}}{\text{mol}}\right)}{\text{Heat capacity } \left(\frac{\text{J}}{\text{mol}} \times \text{K}\right)}\right) - P^{\text{ol-liq}}(\text{kbar}) \times \frac{\text{d}T}{\text{d}P}\left(\frac{\text{K}}{\text{kbar}}\right). \quad (1)$$

where $T^{\text{ol-liq}}$ = 1542°C (taken from the average of T_{eq} from the olivine antecrysts); melt fraction = 0.22; heat of fusion = 130,000 kJ/mol; heat capacity = 192.4 (J/mole×K); $P^{\text{ol-liq}}$ = 8 kbar; and dT/dP assumed to be equal to 0.001 (K bar^{-1}). See Putirka (2008) for details of these experimentally determined parameters.

These calculations imply that the Tissint magma equilibrated last with olivine at ~1680 ± 55°C during late Amazonian (~574 ± 20 Ma; Brennecka et al. 2014). This value is in line with the previously calculated source temperature of ~1700 °C (Putirka 2016) and 1540 ± 10 °C (Musselwhite et al. 2006) for Y-980459, and ~1745 °C for olivine-phyric shergottites in general (Filiberto 2017). This temperature is also comparable to Phanerozoic terrestrial mantle plume heads with a calculated temperature of ~1700 °C (Thompson and Gibson 2000), which matches estimates of the temperature of some modern terrestrial plumes (Putirka 2016). Martian mantle plume temperatures are calculated to be 120 °C hotter than their surrounding

ambient mantle (Li and Kiefer 2007). Thus, a Tissint magma source temperature of ~1680 °C reflects a Martian mantle temperature of ~1560 °C; this value matches precisely the values predicted from stagnant-lid evolution of the Martian mantle (e.g., Spohn 1991; Nimmo and Stevenson 2000; Kiefer 2003; Breuer and Spohn 2006; Parmentier and Zuber 2007). This is also a reasonable value when compared with the average ambient mantle temperature of ~1650 °C for Archean Earth (Green et al. 2001), implying that Mars was able to retain more heat in its interior due to its stagnant-lid regime (in contrast to Earth's plate tectonics) and inefficient cooling of the Martian interior (Hauck and Phillips 2002; Grott and Breuer 2010; Fraeman and Korenaga 2010; Breuher and Spohn 2006; Ruiz et al. 2011; Kiefer 2003).

CONCLUSION

The Tissint-depleted shergottite contains two populations of olivine—large early-crystallizing antecrysts and smaller later crystallizing phenocrysts. Irregular oscillatory zoning of phosphorus is present within both antecrysts and phenocrysts, with P-enriched bands containing up to 0.25 wt% P_2O_5. Mineral chemistry shows no evidence of melt mixing within the magma chamber, thus solute trapping caused by convective crystal movement from hotter to cooler regions of the magma chamber may explain oscillatory zone formation within Tissint olivine.

Olivine equilibration temperatures for the antecryst cores are used to infer the potential temperature of the Tissint source region during the late Amazonian. These calculations suggest a temperature of 1680 °C for the Tissint magma source, and a Martian mantle temperature of 1560 °C—the latter being consistent with the ambient mantle temperature of Archean Earth (~1650 °C, Green et al. 2001). Ultimately, these calculations suggest that the Martian mantle was still active during the late Amazonian, a conclusion that may be confirmed in the future via the ongoing NASA InSight (Interior Exploration using Seismic Investigations, Geodesy and Heat Transport) mission.

Acknowledgments—We are grateful to the Natural History Museum of London for providing the Tissint samples, and to P. Chung and H. Jackson for their help during SEM-EDS and LA-ICP-MS analyses, respectively. The microprobe work was funded by the Australian Research Council via their Australian Laureate Fellowship program awarded to Prof. Phil Bland. The authors acknowledge the facilities, and the scientific and technical assistance, of the Centre for Microscopy, Characterisation and Analysis, University of Western Australia particularly the assistance and expertise provided by Dr. Malcolm Roberts. We also acknowledge funding from STFC grants ST/N000846/1 and ST/H002960/1. We thank Dr. Amy Riches for suggestions relating to the manuscript. We thank Dr. H. McSween and Dr. A. Basu Sarbadhikari for their review of this manuscript.

Editorial Handling—Dr. Michael Zolensky

REFERENCES

Armstrong J. T. 1988. Quantitative analysis of silicates and oxide minerals: Comparison of Monte-Carlo, ZAF and Phi-Rho-Z procedures. *Microbeam Analysis* 59:239–246.

Aziz M. J. 1982. Model for solute redistribution during rapid solidification. *Journal of Applied Physics* 53(2):1158–1168.

Balta J. B., Sanborn M., McSween H. Y., and Wadhwa M. 2013. Magmatic history and parental melt composition of olivine-phyric shergottite LAR 06319: Importance of magmatic degassing and olivine antecrysts in Martian magmatism. *Meteoritics & Planetary Science* 48:1359–1382.

Balta J. B., Sanborn M. E., Udry A., Wadhwa M., and McSween H. Y. 2015. Petrology and trace element geochemistry of Tissint, the newest shergottite fall. *Meteoritics & Planetary Science* 50:63–85.

Barton M., Varekamp J. C., and Van M. J. 1982. Complex zoning of clinopyroxenes in the lavas of vulsini, latium, Italy: Evidence for magma mixing. *Journal of Volcanology and Geothermal Research* 14:361–388.

Basu Sarbadhikari A. B., Babu E. V. S. S. K., Kumar T. V., and Chennaoui Aoudjehane H. 2016. Martian meteorite Tissint records unique petrogenesis among the depleted shergottites. *Meteoritics & Planetary Science* 51:1588–1610.

Basu Sarbadhikari A., Babu E. V. S. S. K., and Vijaya Kumar T. 2017. Chemical layering in the upper mantle of Mars: Evidence from olivine-hosted melt inclusions in Tissint. *Meteoritics & Planetary Science* 52:251–267.

Beattie P. 1993. Olivine-melt and orthopyroxene-melt equilibria. *Contributions to Mineralogy and Petrology* 115:103–111.

Berman D. C. and Hartmann W. K. 2002. Recent fluvial, volcanic, and tectonic activity on the Cerberus Plains of Mars. *Icarus* 159:1–17.

Bouvet de Maisonneuve C., Costa F., Huber C., Vonlanthen P., Bachmann O., and Dungan M. A. 2016. How do olivines record magmatic events? Insights from major and trace element zoning. *Contributions to Mineralogy and Petrology* 171:56.

Brennecka G. A., Borg L. E., and Wadhwa M. 2014. Insights into the Martian mantle: The age and isotopics of the meteorite fall Tissint. *Meteoritics & Planetary Science* 49:412–418.

Breuer D. and Spohn T. 2006. Viscosity of the Martian mantle and its initial temperature: Constraints from crust formation history and the evolution of the magnetic field. *Planetary and Space Science* 54:153–169.

Carey R. J., Manga M., Degruyter W., Gonnermann H., Swanson D., Houghton B., Orr T., and Patrick M. 2013. Convection in a volcanic conduit recorded by bubbles. *Geology* 41:395–398.

Carr M. H. and Head J. W. III 2010. Geologic history of Mars. *Earth and Planetary Science Letters* 294:185–203.

Castle N. and Herd C. D. K. 2017. Experimental petrology of the Tissint meteorite: Redox estimates, crystallization curves, and evaluation of petrogenetic models. *Meteoritics & Planetary Science* 52:125–146.

Castle N., and Herd C. D. K. 2018. Experimental investigation into the effects of oxidation during petrogenesis of the Tissint meteorite. *Meteoritics & Planetary Science* 53:1341–1363.

Chennaoui A. H., Avice G., Barrat J. A., Boudouma O., Chen G., Duke M. J. M., Franchi I. A., Gattacceca J., Grady M. M., Greenwood R. C., Herd C. D. K., Hewins R., Jambon A., Marty B., Rochette P., Smith C. L., Sautter V., Verchovsky A., Weber P., and Zanda B. 2012. Tissint Martian meteorite: A fresh look at the interior, surface, and atmosphere of Mars. *Science* 338:785–788.

Cioni R., Marianelli P., and Santacroce R. 1998. Thermal and compositional evolution of the shallow magma chambers of Vesuvius: Evidence from pyroxene phenocrysts and melt inclusions. *Journal of Geophysical Research-Solid Earth* 103:18277–18294.

Clark A. H., Pearce T. H., Roeder P. L., and Wolfson I. 1986. Oscillatory zoning and other microstructures in magmatic olivine and augite: Nomarski interference contrast observations on etched polished surfaces. *American Mineralogist* 71:734–741.

Day J. M. D., Taylor L. A., Floss C., and McSween H. Y. 2006. Petrology and chemistry of MIL 03346 and its significance in understanding the petrogenesis on nakhlites on Mars. *Meteoritics & Planetary Science* 41:581–606.

Davidson J. P., Morgan D. J., Charlier B. L. A., Harlou R., and Hora J. M. 2007. Microsampling and isotopic analysis of igneous rocks: Implications for the study of magmatic systems. *Annual Review of Earth and Planetary Sciences* 35:273–311.

Donovan J. J. and Tingle T. N. 1996. An improved mean atomic number correction for quantitative microanalysis. *Journal of Microscopy* 2:1–7.

Donovan J. J., Snyder D. A., and Rivers M. L. 1993. An improved interference correction for trace element analysis. *Microbeam Analysis* 2:23–28.

Donovan J. J., Singer J. W., and Armstrong J. T. 2016. A new EPMA method for fast trace element analysis in simple matrices. *American Mineralogist* 101:1839–1853.

Downes M. J. 1974. Sector and oscillatory zoning in calcic augites from M. Etna, Sicily. *Contributions to Mineralogy and Petrology* 47:187–196.

Duncan A. M. and Preston R. M. F. 1980. Chemical variation of clinopyroxene phenocrysts from the trachybasaltic lavas of Mount Etna, Sicily. *Mineralogical Magazine* 43:765–770.

Elardo S. M. and Shearer C. K. 2014. Magma chamber dynamics recorded by oscillatory zoning in pyroxene and olivine phenocrysts in basaltic lunar meteorite Northwest Africa 032. *American Mineralogist* 99:355–368.

Ennis M. E. and McSween H. Y. 2014. Crystallization kinetics of olivine-phyric shergottites. *Meteoritics & Planetary Science* 49:1440–1455.

Eriksson S. C. 1985. Oscillatory zoning in clinopyroxenes from the Guide Copper Mine, Phalaborwa, South-Africa. *American Mineralogist* 70:74–79.

Filiberto J. 2017. Geochemistry of Martian basalts with constraints on magma genesis. *Chemical Geology* 466:1–14.

Fraeman A. A. and Korenaga J. 2010. The influence of mantle melting on the evolution of Mars. *Icarus* 210:43–57.

Ginibre C., Kronz A., and Worner G. 2002. High-resolution quantitative imaging of plagioclase composition using accumulated backscattered electron images: New constraints on oscillatory zoning. *Contributions to Mineralogy and Petrology* 142:436–448.

Grant T. B. and Kohn S. C. 2013. Phosphorus partitioning between olivine and melt: An experimental study in the system Mg_2SiO_4-$Ca_2Al_2Si_2O_9$-$NaAlSi_3O8$-$Mg_3(PO_4)_2$. *American Mineralogist* 98:1860–1869.

Green D. H., Falloon T. J., Eggins S. M., and Yaxley G. M. 2001. Primary magmas and mantle temperatures. *European Journal of Mineralogy* 13:437–451.

Grott M. and Breuer D. 2010. On the spatial variability of the martian elastic lithosphere thickness: evidence for mantle plumes? *Journal of Geophysical Research* 115:E03005.

Hallis L. J., Huss G. R., Nagashima K., Taylor G. J., Stoffler D., and Lee M. R. 2017. Effects of shock and Martian alteration on Tissint hydrogen isotope ratios and water content. *Geochimica et Cosmochimica Acta*. 200:280–294.

Hauck S. A. and Phillips R. J. 2002. Thermal and crustal evolution of Mars. *Journal of Geophysical Research* 107: E7.

Herd C. D. K., Duke M. J. M., Bryden C. D., and Pearson D. G. 2013. Tissint among the shergottites: Parental melt composition, redox state, La/Yb and V/Sc (abstract #1719). 44th Lunar and Planetary Science Conference. CD-ROM.

Hollister L. S. and Hargraves R. B. 1970. Compositional zoning and its significance in pyroxenes from two coarse grained Apollo 11 samples. Apollo 11 Lunar Science Conference. pp. 541-550.

Irving A. J., Kuehner S. M., Tanaka R., Herd C. D. K., Chen G., and Lapen T. J. 2012. The Tissint depleted permafic olivine-phyric shergottite: Petrologic, elemental, and isotopic characterization of a recent Martian fall in Morocco (abstract). *Meteoritics & Planetary Science* 47:2010.

Jean M. M., McCanta M., Howarth G. H., and Taylor L. A. 2017. The Martian olivine glossary: Common textures and zoning patterns, and implications for ascent of Martian magmas and their plumbing systems (abstract #2067). 48th Lunar and Planetary Science Conference. CD-ROM.

Jerram D. A. and Martin V. M. 2008. Understanding crystal populations and their significance through the magma plumbing system. *Geological Society of London Special Publication* 304:133–148.

Kiefer W. S. 2003. Melting in the Martian mantle: Shergottite formation and implications for present-day mantle convection on Mars. *Meteoritics & Planetary Science* 39:1815–1832.

Kinzler R. J. and Grove T. L. 1992. Primary magmas of mid-ocean ridge basalts 1. Experiments and methods. *Journal of Geophysical Research* 97:6885–6906.

Li Q. and Kiefer W. S. 2007. Mantle convection and magma production on present-day Mars: Effects of temperature-dependent rheology. *Geophysical Research Letters* 34: L16203.

Liu J., Liu Q. Y., Guo B., Yuen D. A., and Song H. Z. 2007. Small-scale convection in the upper mantle beneath the Chinese Tian Shan Mountains. *Physics of the Earth and Planetary Interiors* 163:179–190.

Liu Y., Baziotis I. P., Asimow P. D., Bodnar R. J., and Taylor L. A. 2016. Mineral chemistry of the Tissint

meteorite: Indications of two-stage crystallization in a closed system. *Meteoritics & Planetary Science* 51:2293–2315.

Lofgren G. E., Huss G. R., and Wasserburg G. J. 2006. An experimental study of trace-element partitioning between Ti-Al-clinopyroxene and melt: Equilibrium and kinetic effects including sector zoning. *American Mineralogist* 91 (10):1596–1606.

Martin D., Griffiths R. W., and Campbell I. H. 1987. Compositional and thermal convection in magma chambers. *Contributions to Mineralogy and Petrology* 96:465–475.

McCanta M. C., Beckett J. R., and Stolper E. M. 2016. Correlations and zoning patterns of phosphorus and chromium in olivine from H chondrites and the LL chondrite Semarkona. *Meteoritics & Planetary Science* 51:520–546.

McSween H. Y. Jr. 2002. The rocks of Mars, from far and near. *Meteoritics & Planetary Science* 37:7–25.

Meado A. L., Schwenzer S. P., Hammond S. J., and Filiberto J. 2017. Crystallization history of gabbroic shergottite NWA 6963 as revealed by pyroxene zoning (abstract #1504). 48th Lunar and Planetary Science Conference. CD-ROM.

Mikouchi T., Miyamoto M., and McKay G. A. 1999. The role of undercooling in producing igneous zoning trends in pyroxenes and maskelynites among basaltic Martian meteorites. *Earth and Planetary Science Letters* 173:235–256.

Milman-Barris M. S., Beckett J. R., Baker M. B., Hofmann A. E., Morgan Z., Crowley M. R., Vielzeuf D., and Stolper E. 2008. Zoning of phosphorus in igneous olivine. *Contributions to Mineralogy and Petrology* 155:739–765.

Miyamoto M., Duke M. B., and McKay D. S. 1985. Chemical zoning and homogenization of Pasamonte-type pyroxene and their bearing on thermal metamorphism of a howardite parent body. *Journal of Geophysical Research* 90:C629–C635.

Moussallam Y., Oppenheimer C., Scaillet B., Buisman I., Kimball C., Dunbar N., Burgisser A., Chipper C. I., Andujar J., and Kyle P. 2015. Megacrystals track magma convection between reservoir and surface. *Earth and Planetary Science Letters* 413:1–12.

Musselwhite D. S., Dalton H. A., Kiefer W. S., and Treiman A. H. 2006. Experimental petrology of the basaltic shergottite Yamato-980459: Implications for the thermal structure of the Martian mantle. *Meteoritics & Planetary Science* 41:1271–1290.

Nimmo F. and Stevenson D. J. 2000. Influence of early plate tectonics on the thermal evolution and magnetic field of Mars. *Journal of Geophysical Research* 105:11,969–11,979.

Nyquist L. E., Bogard D. D., Shih C. Y., Greshake A., Stoffler D., and Eugster O. 2001. Ages and geologic histories of Martian meteorites. *Chronology and Evolution of Mars* 96:105–164.

Parmentier E. M. and Zuber M. T. 2007. Early evolution of Mars with mantle compositional stratification or hydrothermal crustal cooling. *Journal of Geophysical Research* 112:E02007.

Pearce T. H. 1994. Recent work on oscillatory zoning in plagioclase. *Feldspars and Their Reactions* 421:313–349.

Pearce T. H. and Kolisnik A. M. 1990. Observations of plagioclase zoning using interference imaging. *Earth-Science Reviews* 29:9–26.

Poldervaart A. and Hess H. H. 1951. Pyroxenes in the crystallization of basaltic magma. *The Journal of Geology* 59:472–489.

Putirka K. 2008. Thermometers and barometers for volcanic systems. *Review in Mineralogy and Geochemistry* 69:61–120.

Putirka K. 2016. Rates and style of planetary cooling on Earth, Moon, Mars and Vesta, using new models for oxygen fugacity, ferric-ferrous ratios, olivine-liquid Fe-Mg exchange, and mantle potential temperature. *American Mineralogist* 101:819–840.

Putirka K. D., Perfit M., Ryerson F. J., and Jackson M. G. 2007. Ambient and excess mantle temperatures, olivine thermometry, and active vs. passive upwelling. *Chemical Geology* 241:177–206.

Reitano R., Smith P. M., and Aziz M. J. 1994. Solute trapping of Group-III, IV, and V elements in silicon by an aperiodic stepwise growth-mechanism. *Journal of Applied Physics* 76:1518–1529.

Reubi O., Nicholls I. A., and Kamenetsky V. S. 2003. Early mixing and mingling in the evolution of basaltic magmas: evidence from phenocryst assemblages, Slamet Volcano, Java, Indonesia. *Journal of Volcanology and Geothermal Research* 119:255–274.

Rhodes J. M., Dungan M. A., Blanchard D. P., and Long P. E. 1979. Magma mixing at mid-ocean ridges: Evidence from basalts drilled near 22 degree on the Mid-Atlantic Ridge. *Tectonophysics* 55:35–61.

Roeder P. L. and Emslie R. F. 1970. Olivine-liquid equilibrium. *Contributions to Mineralogy and Petrology* 29:275–289.

Ruiz J., McGovern P. J., Jiménez-Díaz A., López V., Williams J. P., Hahn B. C., and Tejero R. 2011. The thermal evolution of Mars as constrained by paleo-heat flows. *Icarus* 215:508–517.

Scott P. W. 1980. Zoned pyroxenes and amphiboles from camptonites near Gran, Oslo region, Norway. *Mineralogical Magazine* 43:913–917.

Shearer C. K., Aaron P. M., Burger P. V., Guan Y., Bell A. S., and Papike J. J. 2013. Petrogenetic linkages among fO2, isotopic enrichments-depletions and crystallization history in Martian basalts: Evidence from the distribution of phosphorus in olivine megacrysts. *Geochimica et Cosmochimica Acta* 120:17–38.

Sheehan F. and Barclay J. 2016. Staged storage and magma convection at Ambrym volcano, Vanuatu. *Journal of Volcanology and Geothermal Research* 322:144–157.

Shore M. and Fowler A. D. 1996. Oscillatory zoning in minerals: a common phenomenon. *Canadian Mineralogist* 34:1111–1126.

Simonetti A., Shore M., and Bell K. 1996. Diopside phenocrysts from nephelinite lavas, Napak volcano, eastern Uganda: Evidence for magma mixing. *Canadian Mineralogist* 34:411–421.

Spear F. S. and Markussen J. C. 1997. Mineral zoning, P-T–X–M phase relations, and metamorphic evolution of some Adirondack Granulites, New York. *Journal of Petrology* 38:757–783.

Spohn T. 1991. Mantle differentiation and thermal evolution of Mars, Mercury, and Venus. *Icarus* 90:222–236.

Stevenson D. J., Spohn T., and Schubert G. 1983. Magnetism and thermal evolution of the terrestrial planets. *Icarus* 54:466–489.

Stöffler D., Keil K., and Scott E. R. D. 1991. Shock metamorphism of ordinary chondrites. *Geochimica & Cosmochimica Acta* 55:3845–3867.

Takeuchi H. and Sugi N. 1971. Polar wandering and mantle convection. *International Astronomical Union Symposium* 48:212.

Thompson R. N. 1972. Oscillatory and sector zoning in augite from a Vesuvian lava. *Carnegie Institution of Washington Yearbook* 71:463–470.

Thompson R. N. and Gibson S. A. 2000. Transient high temperatures in mantle plume heads inferred from magnesian olivines in Phanerozoic picrites. *Nature* 407:502–506.

Toplis M. J., Libourel G., and Carroll M. R. 1994. The role of phosphorus in crystallisation processes of basalt: an experimental study. *Geochimica & Cosmochimica Acta* 58:797–810.

Walton E. L., Sharp T. G., Hu J., and Filiberto J. 2014. Heterogeneous mineral assemblages in Martian meteorite Tissint as a result of a recent small impact event on Mars. *Geochimica et Cosmochimica Acta* 140:334–348.

Watson E. B., Cherniak D. J., and Holycross M. E. 2015. Diffusion of phosphorus in olivine and molten basalt. *American Mineralogist* 100:2053–2065.

Yoder C. F., Konopliv A. S., Yuan D. N., Standish E. M., and Folkner W. M. 2003. Fluid core size of Mars from detection of the solar core. *Science* 300:299–303.

SUPPORTING INFORMATION

Additional supporting information may be found in the online version of this article.

Supplementary Material 1. Averages major elements of phases in Tissint

Supplementary Material 2. Olivine and chromite chemistry.